Electronic Supplementary Material (ESI) for Nanoscale.

Supplementary Materials

Coupling nanobubbles in 2D lateral heterostructures

Sharad Ambardar[a], Rana Kamh[b], Zachary H. Withers[c], Prasana K. Sahoo[d], and Dmitri V. Voronine[a,c,*]

[a]*Department of Medical Engineering, University of South Florida, Tampa, FL 33620*
[b]*Department of Electrical Engineering, University of South Florida, Tampa, FL 33620*
[c]*Department of Physics, University of South Florida, Tampa, FL 33620*
[d]*Materials Science Centre, India Institute of Technology, Kharagpur, India*

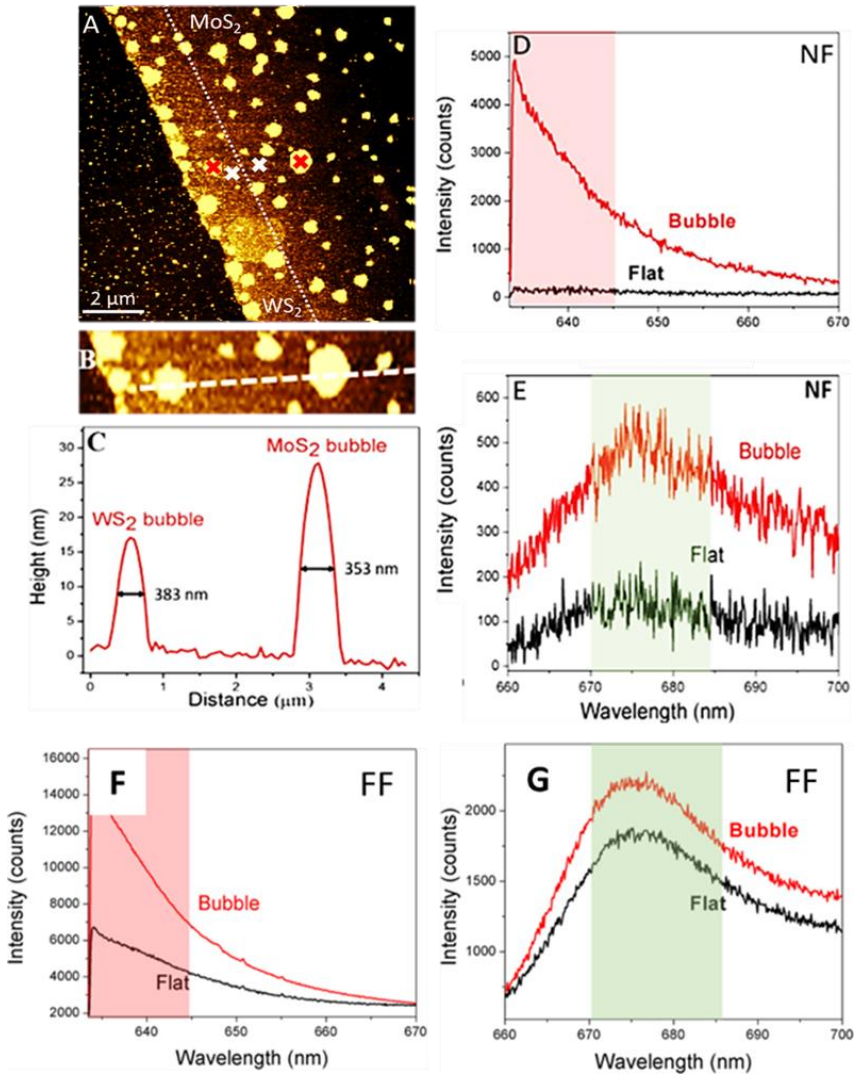

Figure S1. (A) AFM height image of a monolayer lateral MoS_2-WS_2 heterostructure on a SiO_2/Si substrate. The white dashed line in (A) indicates the junction between MoS_2 and WS_2. (B) AFM height image of the zoomed-in area, which includes WS_2 and MoS_2 nanobubbles marked by red crosses in (A), which are referred to as W1 and Mo1, respectively. (C) AFM height profile of the bubbles, which corresponds to the white dashed line in (B). Near-field (NF) PL spectra on WS_2 (D) and MoS_2 (E). Far-field (FF) PL spectra on the bubble and flat areas on WS_2 (F) and MoS_2 (G) indicated by red and white crosses in (A), respectively.

1. **Contrast factors**

We calculated contrast factors (CF) to simplify the effects of coupling by

$$\mathrm{CF} = \frac{I_{NF}}{I_{FF}} - 1$$

where I_{FF} and I_{NF} were calculated by taking the far-field (FF) and near-field (NF) intensity average of the area integrated within the FWHM of the bubble, respectively.

Contrast Factor	***WS_2 (W1)***	***MoS_2 (Mo1)***	***WS_2 (W2)***	***MoS_2 (Mo2)***
CF	-0.7	-0.9	-1.1	-0.4

Table S1. Contrast factors (CF) for the uncoupled bubbles WS_2 (W1) and MoS_2 (Mo1) shown in Figure 3, and for the coupled bubbles WS_2 (W2) and MoS_2 (Mo2) in Figure 4.

2. Theoretical Model

2.1 TEPL of uncoupled MoS_2 and WS_2

Figure S10A shows the theoretical model that we developed to describe the tip-sample distance dependence of the uncoupled pure MoS_2 and WS_2 materials without nanobubbles as three-level systems based on our previous model of TEPL in $MoSe_2$-WSe_2 heterostructures[1]. The PL signal is proportional to the population of exciton state $|X\rangle$, which is coupled to a higher state $|X^0\rangle$ and the ground state $|g\rangle$. The rate equations for the corresponding state populations N_X, N_{X0} and N_g are given by

$$\frac{dN_g}{dt} = -\Gamma_p(d)N_g + \frac{N_X}{\tau_X}, \tag{S1}$$

$$\frac{dN_X}{dt} = \alpha N_{X0} - \frac{N_X}{\tau_x}, \tag{S2}$$

$$N_g + N_X + N_{X0} = 1, \tag{S3}$$

where α is the $|X\rangle$ exciton generation rate. The tip-sample distance dependent near-field excitation rate is given by[1,2]

$$\Gamma_p(d) = \begin{cases} A\left(1 - \frac{B}{(R+d-c)^3}\right)^{-2}, & \text{for d} > 0.36 \text{ nm} \\ 1 - e^{-\frac{d-c}{d_p}}, & \text{for } c < \text{d} < 0.36 \text{ nm} \end{cases}, \tag{S4}$$

where A is a constant for continuity of the piecewise function, $B = 5028$ characterizes the probe's material properties[1,2], $R = 20$ nm is the radius of curvature of the tip apex, $c = 0.17$ nm is the ohmic conduction distance, and $d_p = 0.02$ nm is the average quantum tunneling distance[1]. The exciton generation rate $\alpha = 1\ ps^{-1}$ and the average exciton lifetime $\tau_X = 2\ ps$ were used. The tip-sample distance dependence of the N_X population in steady state using these parameters is shown in Fig. S10B.

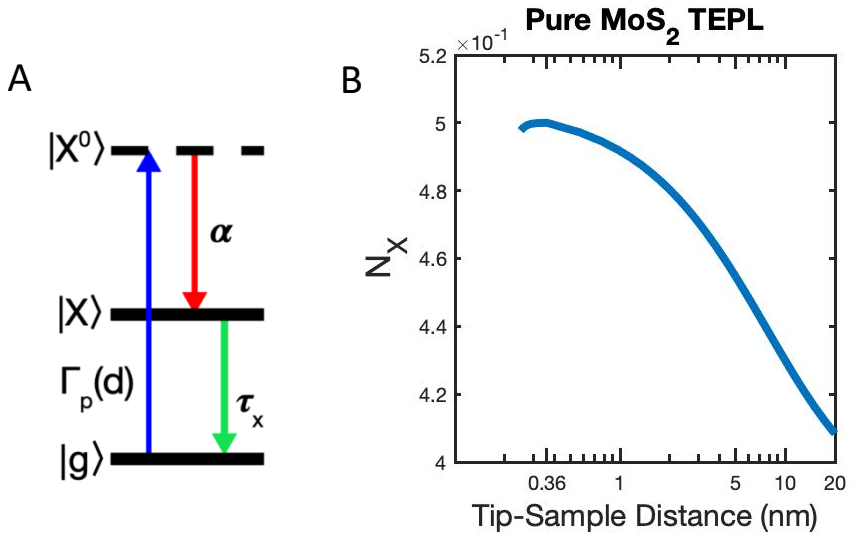

Figure S2. (A) Phenomenological model diagram of exciton dynamics in uncoupled pure MoS_2 and WS_2 materials. (B) Simulated tip-sample distance dependence of exciton population in pure MoS_2.

2.2 TEPL of coupled MoS_2 and WS_2

Figure S3A shows the theoretical model that we developed to describe the tip-sample distance dependence of the coupled MoS_2 and WS_2 nanobubbles based on the combination of our previous models of $MoSe_2$-WSe_2[1] and MoS_2-WS_2[3] heterostructures without nanobubbles. The PL signals of MoS_2 and WS_2 are proportional to the populations of exciton states $|X\rangle$ and $|Y\rangle$, respectively, which are coupled to the ground state $|g\rangle$, and the corresponding higher states $|X^0\rangle$ and $|Y^0\rangle$. The rate equations for the state populations N_g, N_{X0}, N_{Y0}, N_X, and N_Y are given by

$$\frac{dN_g}{dt} = -2\Gamma_p(d)N_g + \frac{N_X}{\tau_X} + \frac{N_Y}{\tau_Y}, \tag{S5}$$

$$\frac{dN_X}{dt} = \alpha N_{X0} - \frac{N_X}{\tau_x} + \gamma_1\Gamma_p(d)N_Y, \tag{S6}$$

$$\frac{dN_Y}{dt} = \beta N_{Y0} - \frac{N_Y}{\tau_Y} - \gamma_1\Gamma_p(d)N_Y, \tag{S7}$$

$$\frac{dN_{X0}}{dt} = \Gamma_p(d)N_g - \alpha N_{X0} - \gamma_2\Gamma_p(d)N_{X0}, \tag{S8}$$

$$N_g + N_X + N_Y + N_{X0} + N_{Y0} = 1, \tag{S9}$$

where α and β are exciton $|X\rangle$ and $|Y\rangle$ generation rates, τ_X and τ_Y are the average exciton lifetimes, and $\Gamma_p(d)$ is the tip-sample distance dependent near-field excitation rate, described above. Similar simulation parameters were used for $\Gamma_p(d)$ as for the uncoupled model. The coupling between the states $|X\rangle$ and $|Y\rangle$ via the junction was modeled by the photoinduced charge transfer rate $\gamma_1\Gamma_p(d)$ (purple arrow in Fig. S3A) as previously described for the nonresonant TEPL of $MoSe_2$-WSe_2[1]. This leads to an increasing N_X for the decreasing tip-sample distance as shown in Fig. S3B. Similarly, the coupling between the states $|X^0\rangle$ and $|Y^0\rangle$ via the junction was modeled by the photoinduced charge transfer rate $\gamma_2\Gamma_p(d)$ (blue arrow in Fig. S3A) as previously described for the resonant TEPL of MoS_2-WS_2[3]. This leads to an increasing N_Y for the decreasing tip-sample distance (not shown) similar to N_X. This model agrees with our experimental observations for the bubble-junction coupling. For both bubbles coupled to each other via the junction we set $\gamma_2 = 0$ and use $\gamma_1(d_1 = 0) = 0.278$ instead of γ_1' because the effects from the presence of the bubbles at the junction cannot be ignored. This leads to quenching of N_Y (Fig. S3C).

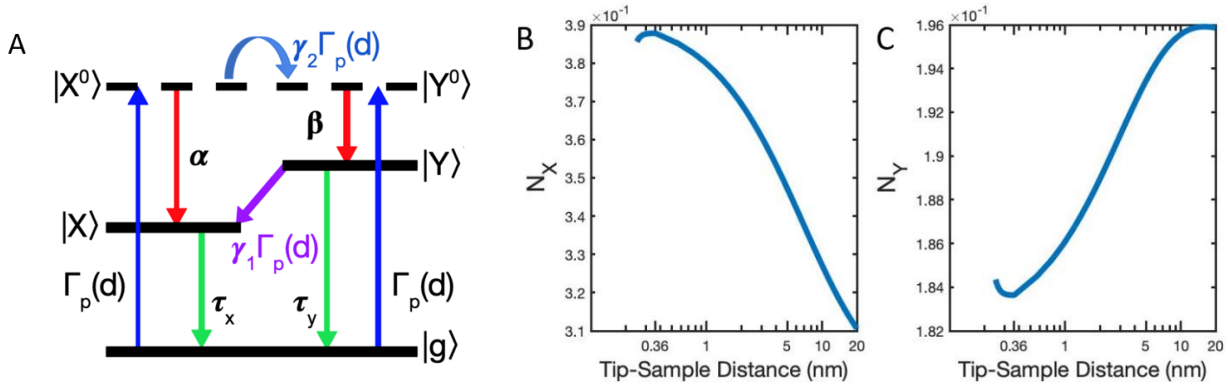

Figure S3. (A) Phenomenological model diagram of exciton dynamics in coupled MoS_2 and WS_2 nanobubbles in the vicinity of the junction in a monolayer MoS_2-WS_2 heterostructure. Simulated tip-sample distance dependence of exciton population in coupled MoS_2 (B) and WS_2 (C) nanobubbles.

The lateral spatial dependence of the effect of the junction width and nanobubbles were described using the following forms of the charge transfer rates

$$\gamma_1(d_1) = \gamma_1'\left(e^{-\frac{1}{2}(\frac{d_1}{\sigma})^2} + e^{-\frac{1}{2}(\frac{d_1-r_1}{\sigma_b})^2}\right), \quad \text{(S10)}$$

and

$$\gamma_2(d_2) = \gamma_2'\left(e^{-\frac{1}{2}(\frac{d_2}{\sigma})^2} + e^{-\frac{1}{2}(\frac{d_2-r_2}{\sigma_b})^2}\right), \quad \text{(S11)}$$

which include the effects of charge funneling due to the shapes of the junction and bubbles approximated by Gaussian functions with the values of the parameters based on the experimental observations. Here, we consider the *bubble-junction coupling* case when either the MoS_2 or WS_2 bubbles are in the vicinity of the junction and are, therefore, coupled to the flat areas of the respective other material. The coupled MoS_2 bubble corresponds to the nonresonant TEPL model of the $MoSe_2$-WSe_2 flat heterostructure[1] and its lateral spatial dependence is described by the d_1 coordinate in the γ_1 rate function in Eq. (S10). Similarly, the coupled WS_2 bubble corresponds to the resonant TEPL model of the MoS_2-WS_2 heterostructure[3] and its lateral spatial dependence is described by the d_2 coordinate in the γ_2 rate function in Eq. (S11) due to the charge tunneling effect. Note that in our model we always assume the junction at the center of the coordinate system with $d_1 = d_2 = 0$, while the bubble is assumed to be on the right side of the junction.

The first term in the left sides of Eqs. (S10) and (S11) describes the shape of the junction with the width of $\sigma = 667\ nm$ based on the experimental TEPL measurements of the junction without bubbles. This width corresponds to the smooth MoS_2->WS_2 junction, that was obtained during the CVD growth of the 2D heterostructures as previously described[4]. This junction width results in the negligible effects ~ 1 μm away from the junction, and approximately corresponds to the far-field spatial resolution of our measurements.

The second term in the left sides of Eqs. (S10) and (S11) describes the shape of the nanobubbles with the positions (r_1 and r_2) and widths (σ_b) obtained from the experiments.

TEPL enhancement factors were simulated by solving Eqs. (S5) - (S11) in steady state as relative enhancements ΔN of MoS_2 (N_X) and WS_2 (N_Y) populations equal to the differences between the corresponding near-field (NF) and far-field (FF) signals at 0.36 nm and 20 nm tip-sample distance, respectively: $\Delta N_X = N_X(0.36nm) - N_X(20nm)$ and $\Delta N_Y = N_Y(0.36nm) - N_Y(20nm)$. The exciton generation rates were $\alpha = \beta = 1\ ps^{-1}$ and the exciton lifetimes were $\tau_X = \tau_Y = 2\ ps$. The coefficients γ_1' and γ_2' were set equal to 0.25 and 1, respectively.

3. TERS of CNT

Figure S4 shows the control experiments of TERS of carbon nanotube (CNT). Figures S4a and S4b are the tip-in and tip-out maps of the G-band integrated intensity of CNT Raman signal. During the tip-in mapping, the tip is in contact-mode with the tip-sample distance (TSD) of 0.3 nm. whereas during the tip-out measurements the TSD is 20 nm. The enhancement factor (EF) was calculated by[5]

$$\mathrm{EF} = \left(\frac{I_{tip-in}}{I_{tip-out}} - 1\right) \mathrm{x}\ \frac{S_{FF}}{S_{NF}},$$

where $\frac{S_{FF}}{S_{NF}}$ is the surface area scaling factor of ~ 2500. The EF ≈ 3537 was obtained.

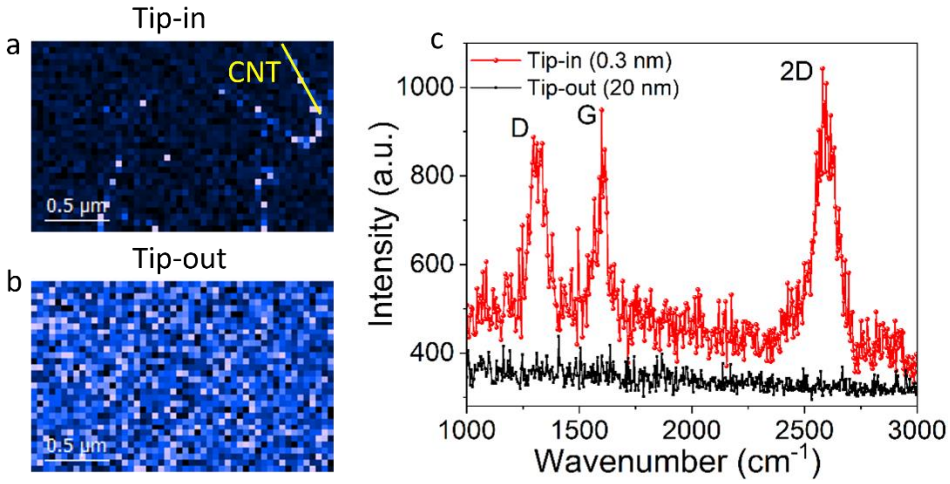

Figure S4. TERS measurements of CNT (marked by yellow solid line). Integrated intensity of the G-band of CNT with tip in contact (a) and tip out-of-contact (b), with the corresponding Raman spectra (c).

4. TERS of W1 (WS_2) and Mo1 (MoS_2) nanobubbles

Both TERS (tip-in) and FF Raman (tip-out) measurements were recorded with 532 nm laser on the bubbles W1 (WS_2) and Mo1 (MoS_2) and their adjacent flat regions.

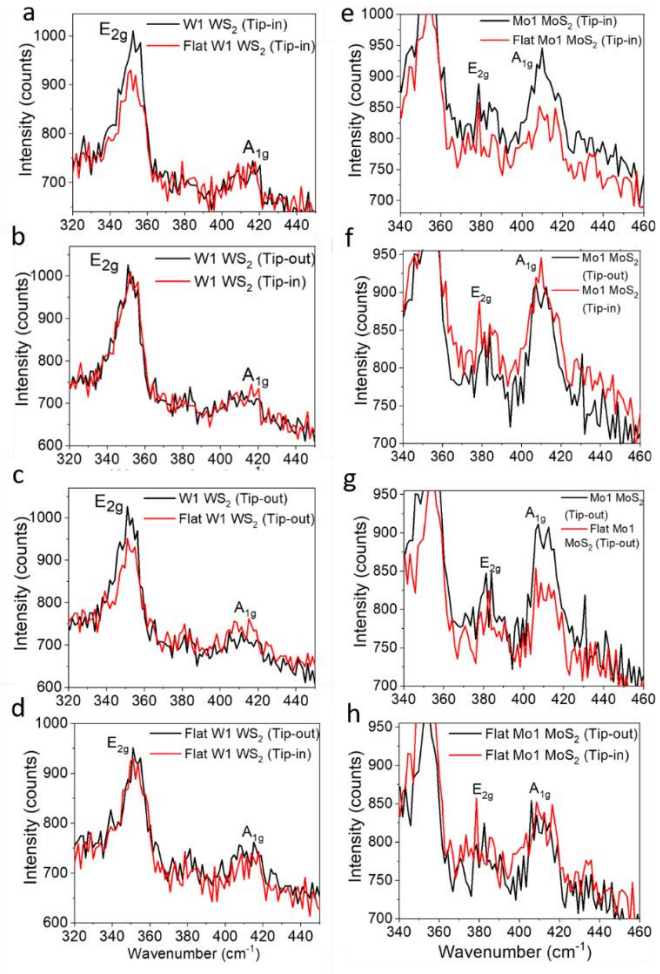

Figure S5. Raman spectra of W1 (WS_2) and Mo1 (MoS_2) shown by red arrows and the corresponding flat areas shown by black arrows in Fig. S1A. (a - d) Far-field and tip-enhanced Raman measurements on WS_2 nanobubble (W1) and its corresponding flat area. (e - h) Far-field and tip-enhanced Raman measurements on MoS_2 (Mo2) nanobubble and its corresponding flat area.

5. TERS of particles

Both TERS (tip-in) and FF Raman (tip-out) measurements were recorded with 532 nm laser on the random particle P shown in Fig. 4. Both spectra show the E^1_{2g} and A_{1g} modes of MoS_2 due to the FF Raman response of the MoS_2 material in the vicinity of the particle. No NF signal enhancement was observed.

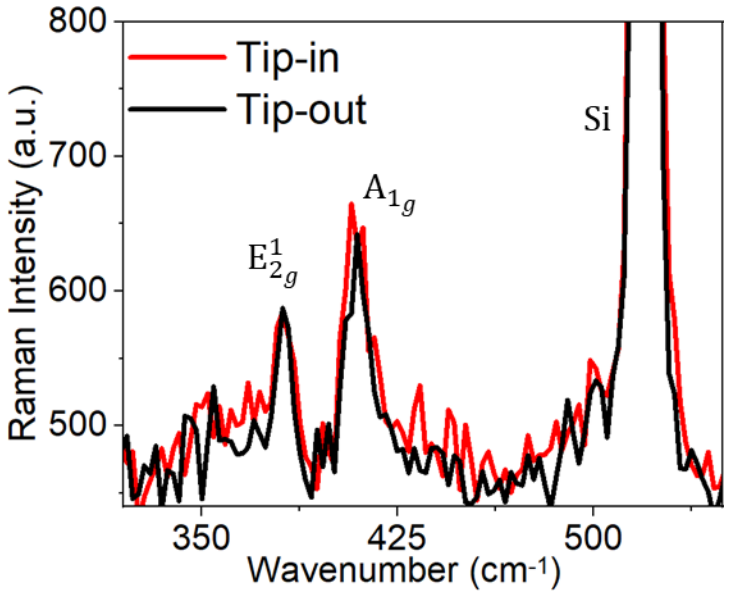

Figure S6. TERS (tip-in) and far-field Raman (tip-out) measurements of the random particle P shown in Fig. 4.

6. Raw data for EF profile calculations

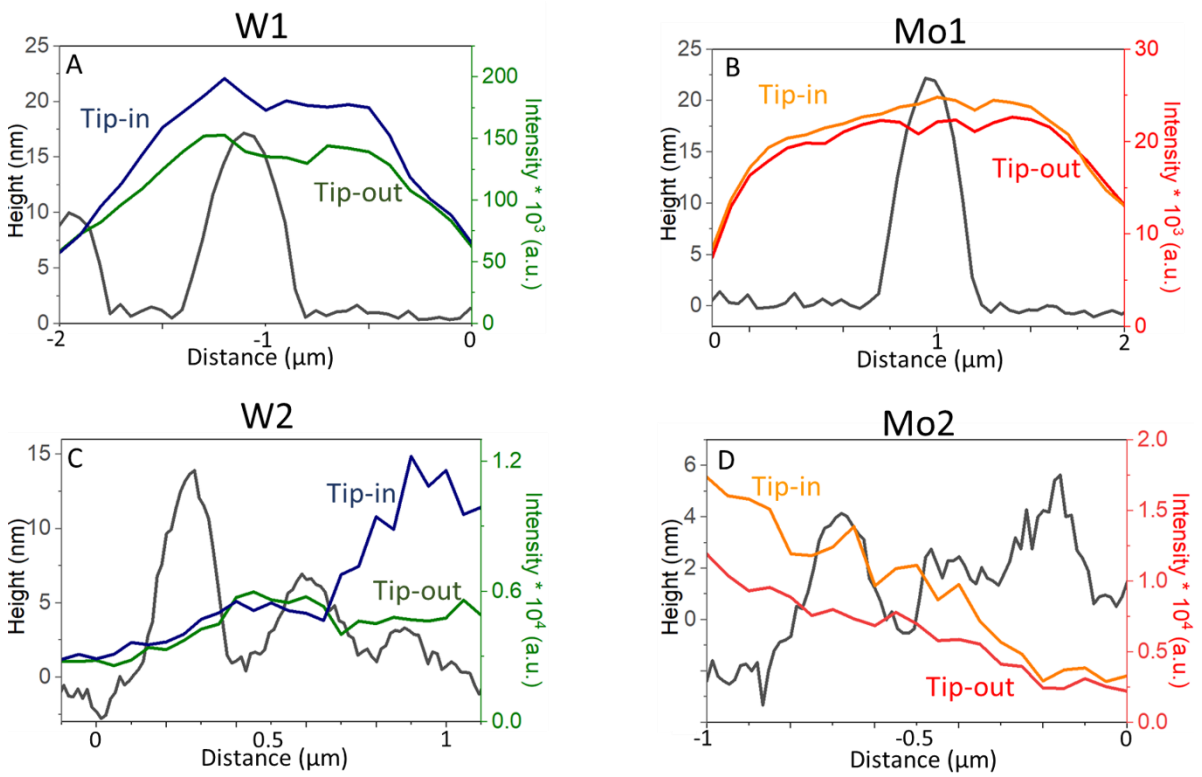

Figure S7. Raw intensity data for EF profile calculations for W1 (A) and Mo1 (B) bubbles in Figures 3d and 3e, respectively; and for W2 (C) and Mo2 (D) bubbles in Figures 4d and 4e, respectively, with (Tip-In) and without (Tip-Out) tip-sample contact.

7. Material characterization

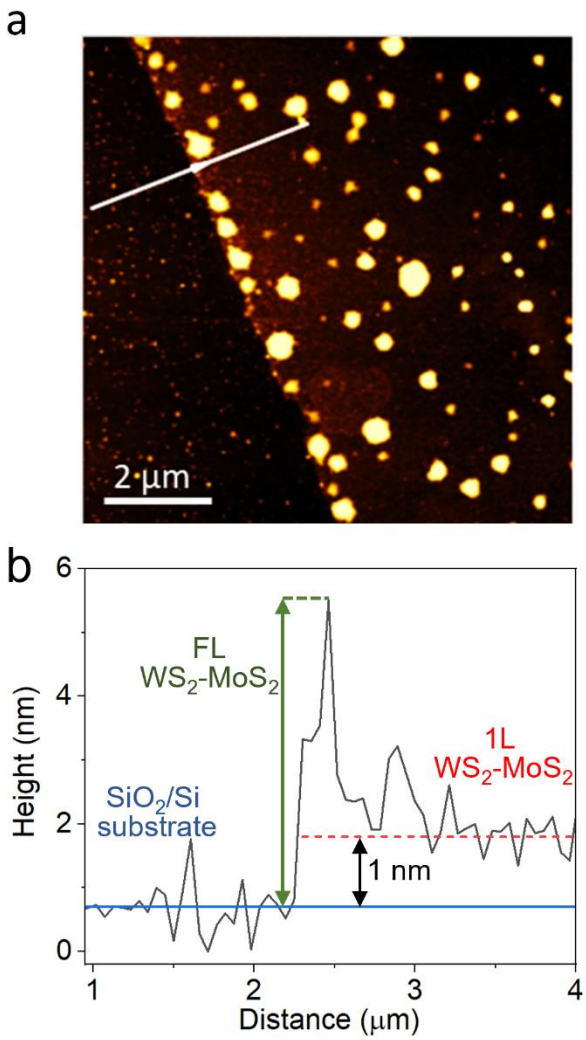

Figure S8. (A) AFM height image of a monolayer lateral MoS_2-WS_2 heterostructure on a SiO_2/Si substrate. (B) AFM profile along the white arrow in (A) shows average monolayer (1L) thickness of < 1 nm. The small few-layer (FL) region at the edge of the heterostructure is typically found in CVD-grown samples.

8. High power damage analysis

Optical characterization of MoS_2-WS_2 heterostructure before and after high power measurements shows the absence of any damage effects.

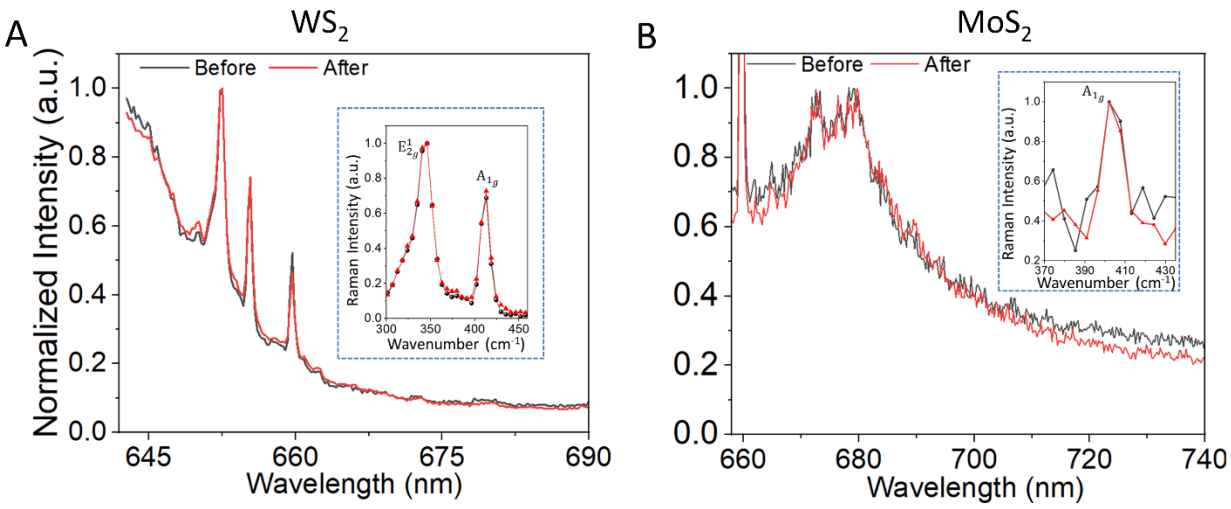

Figure S9. Raman and PL spectra of WS_2 (A) and MoS_2 (B) before (black line) and after (red line) high power measurements.

References

1 C. Tang, Z. He, W. Chen, S. Jia, J. Lou and D. V. Voronine, *Phys. Rev. B*, 2018, **98**, 041402.

2 K.-D. Park, O. Khatib, V. Kravtsov, G. Clark, X. Xu and M. B. Raschke, *Nano Lett.*, 2016, **16**, 2621–2627.

3 Z. H. Withers, S. Ambardar, X. Lai, J. Liu, A. Zhukova and D. V. Voronine, *ArXiv Prepr. ArXiv200110138*.

4 P. K. Sahoo, S. Memaran, Y. Xin, L. Balicas and H. R. Gutiérrez, *Nature*, 2018, **553**, 63–67.

5 Y. Zhang, D. V. Voronine, S. Qiu, A. M. Sinyukov, M. Hamilton, Z. Liege, A. V. Sokolov, Z. Zhang and M. O. Scully, *Sci. Rep.*, 2016, **6**, 1–9.